

# Internal wave band eddy fluxes above a continental slope

by Johannes R. Gemmrich<sup>1,2</sup> and Hans van Haren<sup>1</sup>

## ABSTRACT

Three weeks of velocity and temperature measurements from the bottom 45 m above the continental slope in the Bay of Biscay are used to evaluate the role of the internal wave band in boundary mixing near a sloping bottom. Utilizing acoustic Doppler current profilers and thermistor strings, internal wave band eddy fluxes of momentum and heat are estimated. The instrumentation is specifically designed to resolve internal wave band processes. Due to unresolved Doppler shifting, this wave band may include turbulence as well as internal waves. A very energetic and highly variable near-bottom environment is found. Periods of mixing and restratification alternate at the  $M_2$  tidal frequency. Interpreting the observations in an Ekman sense, the three-week mean current is downwelling-favorable, which is consistent with existing boundary layer theories. However, a bi-directional flow associated with sloping boundary mixing is not found in the near-bottom layer, possibly due to observed strong stratification all the way to the bottom.

We evaluated boundary layer dynamics and the effect of internal wave-band fluxes from two frequency ranges ( $\sigma \geq 15$  cpd and  $\sigma \geq 1.9$  cpd, including tides) on the three-week mean flow. The high-frequency range ( $\sigma \geq 15$  cpd) of the internal wave band supports significant momentum and buoyancy fluxes while the low-frequency range ( $\sigma \geq 1.9$  cpd) only supports significant momentum fluxes. Mean bottom-normal eddy diffusivities associated with anisotropic, nonlinear internal waves, are negative and  $O(-10^{-2} \text{ m}^2 \text{ s}^{-1})$ . Interpreting these negative eddy diffusivities as indication of a restratification process, high mixing efficiencies are expected throughout the mixing layer, which extends typically 20 m above the bottom. Mean eddy viscosities are positive in cross-slope direction and negative in alongslope direction, implying a strong anisotropy in the interaction between internal wave band eddies and the mean flow. Alongslope momentum is transferred from the internal tide to the mean flow. Buoyancy and pressure gradient forces, which we could not determine directly, may generate a buoyancy-driven secondary flow. The buoyancy equation is dominated by advection, possibly balanced by divergence of cross-slope and alongslope internal wave band fluxes.

## 1. Introduction

The dynamics of the boundary layer above a sloping bottom is expected to be profoundly different from that over a flat bottom (Phillips *et al.*, 1986). Buoyancy forces in an inclined boundary layer allow mixed fluid to spread into the pycnocline (Phillips *et al.*, 1986). Thus, boundary layer mixing near a slope is expected to play an important role in

1. Netherlands Institute for Sea Research (NIOZ), P.O. Box 59, 1790 AB Den Burg, Texel, The Netherlands.

2. Present address: Institute of Ocean Sciences, P.O. Box 6000, Sidney, BC, Canada, V8L 4B2. **email:** [gemmrichj@pac.dfo-mpo.gc.ca](mailto:gemmrichj@pac.dfo-mpo.gc.ca)

diapycnal diffusion in the deep ocean (Munk, 1966; Armi, 1978). The exchange rate of the mixed water of the boundary layer with the ocean interior determines the mixing efficiency (Garrett, 1990). A high mixing efficiency is expected only if the mixing layer is larger than the layer where stratification is continually restored by buoyancy-driven flows. This is unlikely for turbulence generated by bottom friction (Phillips *et al.*, 1986) but might be true for a mixing layer generated by breaking internal waves. Reflection of internal waves at sloping boundaries can lead to turbulent boundary mixing (Eriksen, 1985; Ivey and Nokes, 1989; De Silva *et al.*, 1998). Internal waves reflecting from a sloping boundary preserve their frequency and angle to the vertical upon reflection rather than normal to the boundary. At near critical conditions, when the boundary slope matches the inclination of the group velocity vector of the reflected wave, wave breaking may occur. Recently, microstructure and current measurements near seamounts (Lueck and Mudge, 1997; Toole *et al.*, 1997; Eriksen, 1998) and above rough topography (Polzin *et al.*, 1997) have shown enhanced stratified turbulence, possibly associated with internal wave reflection.

A second role attributed to boundary mixing at a sloping bottom is the generation of an interior residual flow (Garrett, 1991), which is downwelling-favorable, i.e. in the Northern Hemisphere with shallow water to the right. Depending on the strength of this circulation, which is a function of the eddy Prandtl number, the mixing-induced flow can cause rectification of a superimposed tidal interior flow.

Central to the issue of boundary mixing above a slope are profiles of momentum fluxes, buoyancy fluxes, and the related profiles of eddy viscosity and eddy diffusivity. The aim of this study is to resolve these profiles with observations at a continental slope and try to establish dynamical consequences of boundary mixing. Breaking of internal waves is expected to play a major role on the continental slope. Therefore, our analysis will focus on the internal wave band,  $f < \sigma < N$ , where  $\sigma$ ,  $f$ ,  $N$  are wave frequency, local inertial frequency and buoyancy frequency, respectively. A pilot study demonstrated the concept of combining acoustic Doppler current profiler (ADCP) and thermistor string measurements to resolve internal wave band eddy fluxes close to the bottom (van Haren *et al.*, 1994). They applied a direct correlation approach to establish eddy fluxes associated with high-frequency internal waves. For the 5-day pilot experiment on a sloping site off Nova Scotia, they found cross-slope momentum fluxes and, at a single depth, bottom-normal buoyancy fluxes, significantly different from zero.

Here we present results from a 22-day experiment, using improved instrumentation on a continental slope, which is critical for frequencies between semidiurnal tidal frequency and its first harmonic. The internal wave band will be split in two, a high-frequency portion ( $\sigma \rightarrow N$ ), and one including the tides. The effects of these different parts on the mean over the deployment period will be discussed.

## 2. Observational approach

Our goal was to measure variations of all three velocity components as well as temperature fluctuations in the near-bottom region at a continental slope, with a sampling

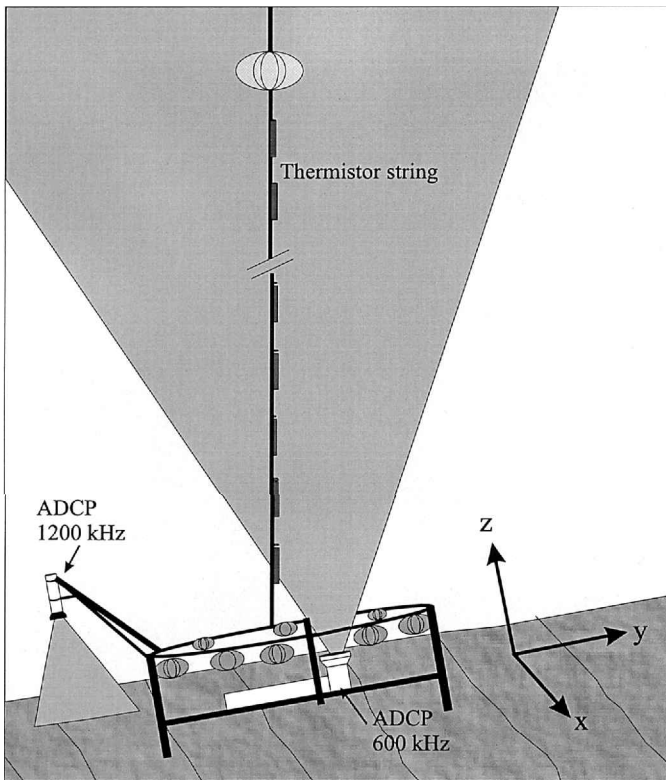


Figure 1. Sketch of instrumentation deployed on a continental slope, also showing the bottom-oriented coordinate system.

rate high enough to resolve the shortest period of the internal wave field, specified by the buoyancy period. For this purpose, a bottom lander was equipped with two ADCPs, a thermistor string and a tiltmeter (Fig. 1). An upward-looking 600-kHz ADCP measured velocities between 4.9 and 47.9 m above the bottom at 1-m intervals. Due to first side lobe interference with the thermistor string data logger, no reliable data were obtained between 31.9 and 33.9 m. A second, downward-looking 1200-kHz ADCP, placed 2.5 m to the side of the 600-kHz ADCP, resolved velocities between 1.04 and 2.04 m at 0.25-m intervals. The beams of the downward-looking ADCP were outside the frame. However, flow distortion due to the bottom lander might influence the velocity readings between 1 and 2 m for readings when the lander is up-stream. The ping frequency was 0.67 Hz for the 600-kHz ADCP and 1.11 Hz for the 1200-kHz ADCP. Data were ensemble-averaged to a sampling rate of once per 30 s, so that the buoyancy period of  $O(30 \text{ min})$  was well resolved. Standard deviation of the horizontal velocities are  $8.6 \times 10^{-3} \text{ m s}^{-1}$  for the 600-kHz ADCP and  $7.6 \times 10^{-3} \text{ m s}^{-1}$  for the 1200-kHz ADCP, per ensemble period. Standard deviations of the vertical components are about four times smaller. A post cruise

calibration check of the 600-kHz ADCP has been carried out to verify the internal coordinate transform performed by the instrument. In particular, the consistency of the crucial vertical velocity as defined in the manufacturers manual and the recorded signal could be confirmed.

Vertical eddy fluxes of alongslope and cross-slope momentum are defined as the covariance of velocity fluctuations,  $\overline{u'w'}$  and  $\overline{v'w'}$ , respectively. Based on a Reynolds decomposition  $u = \bar{u} + u'$ , mean velocities  $\bar{u}$  and fluctuating parts  $u'$  can be obtained after applying a filter with an appropriate cut-off frequency  $\sigma_c$ , and similarly for  $v$  and  $w$ . However, the measurement principle of ADCPs requires additional corrections to estimate momentum fluxes. ADCPs measure Doppler velocities  $b_i$ ,  $i = 1$  to 4, along four slanted beams from which three velocity components  $\hat{u}$ ,  $\hat{v}$  and  $\hat{w}$  are estimated in Cartesian coordinates. Only if the flow field is homogeneous across the beam spread, do these estimates represent the true velocity vector ( $u, v, w$ ). The slant angle  $\theta$ , between the beams and the vertical, is  $\theta = 30^\circ$  for the 1200-kHz ADCP and  $\theta = 20^\circ$  for the 600-kHz ADCP, yielding a beam spread  $>30$  m at the uppermost velocity bin. However, for Reynolds-stress estimates using a four-beam ADCP, it is not necessary that each beam measures the same instantaneous velocity field. Assuming statistical homogeneity of the velocity field (Lohrmann *et al.*, 1990), vertical fluxes of horizontal momentum may be estimated as (van Haren *et al.*, 1994)

$$\overline{u'w'} = \overline{\hat{u}'(\hat{w}' - \hat{e}')} \quad (1)$$

$$\overline{v'w'} = \overline{\hat{v}'(\hat{w}' + \hat{e}')}. \quad (2)$$

The so-called error velocity  $\hat{e}$ , is a measure of current homogeneity over the beam spread and is calculated from the velocity differences obtained by different beam pairs.

$$\hat{e} = \frac{[b_1 + b_2 - (b_3 + b_4)]}{4 \cos \theta}. \quad (3)$$

It is essential for estimating momentum fluxes from ADCP data under the assumption of statistical homogeneity. Error velocities are a standard output of the ADCPs but the recorded values have to be scaled by  $4 \cos \theta$  to match the definition of the true velocity components (van Haren *et al.*, 1994). Furthermore, it can be shown that the vertical Reynolds stress component follows as

$$\frac{\overline{b'_1 b'_3} + \overline{b'_1 b'_4} + \overline{b'_2 b'_3} + \overline{b'_2 b'_4}}{4 \cos^2 \theta} = \overline{w'^2} = \overline{(\hat{w}' + \hat{e}')(\hat{w}' - \hat{e}')}. \quad (4)$$

Vertical turbulent heat fluxes  $\overline{T'w'}$  can be estimated by indirect methods via the dissipation rates of kinetic energy and temperature variance or from the observation of Thorpe (Thorpe, 1987b) and Ozmidov scales. Direct estimation of  $\overline{T'w'}$  are commonly obtained from co-spectra of temperature and vertical velocity (Yamazaki and Osborn, 1993; Fleury and Lueck, 1994; Gargett and Moum, 1995; Sun *et al.*, 1996). Here we are

interested in the contribution to the heat flux by the internal wave band. The role of different frequency bands in supporting a heat flux is estimated by applying two different cut-off frequencies to separate mean and fluctuating signals. We estimate the heat fluxes by employing a direct correlation method  $\overline{T'w'}$ , where fluctuating temperature and velocity signals are restricted to the internal wave frequency band (van Haren *et al.*, 1994). Temperature and velocity measurements are not exactly co-located in our instrumental set-up. An estimate of the resulting error  $\Delta_{Tw}$  suggested by van Haren *et al.* (1994) is given in the Appendix. For our data we find the error to be  $\Delta_{Tw} < 5\%$  of the flux value, and is therefore neglected henceforth. However, the assumption of large eddy sizes compared to the ADCP beam spread may not always be valid. By tracking overturn sizes we estimated conservatively that about half the overturns have larger sizes than the beam spread, so that heat flux estimates may be biased by up to 15% (for details see the Appendix).

The thermistor string, built specifically for internal wave band flux measurements (van Haren *et al.*, 2001), extended over the range 2.9–33.9 m at 1-m resolution. It was located within the beam spread of the upward-looking ADCP. The thermistor string sampling rate matched the sampling of the ADCPs. Synchronous sampling of temperature and velocity field is crucial for calculating heat fluxes. Therefore, the three instrument clocks were synchronized at the beginning of the deployment. Timing errors due to clock drift stayed well within one sampling period. Comparison of temperature signals of thermal fronts (Gemrich and van Haren, 2001) recorded with the internal ADCP thermistors and the closest sensor of the thermistor string confirmed the correct synchronization of the three instruments. The calibration of the individual thermistors is known to within  $\sim 30$  mK. To improve this calibration, temperature offsets of the 32 sensors are determined. During the recovery, all thermistors sample the same water masses. Assuming a constant vertical temperature gradient, as well as a constant rise speed of the thermistor string, the temperature records of the individual sensors can be matched after the temperature differences across the thermistor string have been accounted for. The differences between the matched and recorded temperatures are used to correct the thermistor readings. The maximum offset obtained is 34 mK. However, the mean vertical temperature gradient over the range of the thermistor string does not change after applying this calibration.

Our observations were acquired from June 20 to July 12, 1996 in the Bay of Biscay. We were interested in mixing processes above a sloping bottom associated with the internal wave band. This required a locally smooth bottom topography and a slope comparable to the critical slope of the low-frequency internal wave field. The depth rating of the 1200-kHz ADCP required a deployment site with depth  $< 1000$  m. Eventually, a site ( $48^{\circ}03.8'N$ ,  $8^{\circ}19.9'W$ ) at  $\sim 830$  m isobath had been chosen, based on  $\sim 1800$  echo soundings recorded within  $\pm 10$  km of the deployment site (Fig. 2). Our instrumentation had been deployed on the shoreward side of a large trench. However, within a tidal excursion in along-isobath direction of  $O(3000$  m) the bathymetry is relatively smooth and the slope orientation is well defined.

The slope estimate depends on the horizontal scale which is considered. This scale is

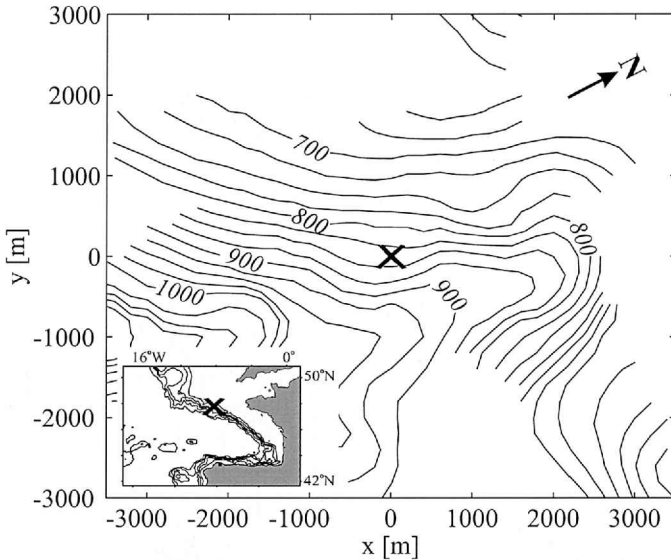


Figure 2. Bathymetry of the deployment site in a slope-oriented coordinate system (isobaths in meters). The cross indicates position of the bottom-lander. Insert: Deployment site in the Bay of Biscay. Isobaths shown are 200 m, 1000 m, 2000 m, 3000 m and 4000 m.

determined by the relevant physical processes, and therefore it is not known *a priori*. For studies on internal wave reflection, the projection of the wave beam width, which is monitored by the vertical profiling range, can provide an appropriate horizontal scale. An upper limit for this scale is given by the cross-isobath distance corresponding to the ADCP profiling depth. In our case, this distance is  $O(500\text{ m})$ , yielding a mean bottom slope  $\alpha = 4.9^\circ$  around the mooring. For a cross-slope scale of 1000 m, the estimated bottom slope increases to  $\alpha_{1000} = 5.2^\circ$ . For smaller scales, the slope estimate slightly decreases. In the following, a bottom-oriented coordinate system is adopted with the  $x$ -direction aligned with the isobaths (alongslope), and the  $y$ -direction across isobaths, positive toward shallower water (cross-slope). The  $z$ -axis is bottom-normal, based on a mean bottom slope  $\alpha = 4.9^\circ$ , and positive upward with the origin at the bottom (Fig. 1).

The buoyancy frequency  $N = 28 \pm 9.5\text{ cpd}$  is estimated from two CTD profiles taken at the beginning of the measurement period within 1500 m of the deployment site, excluding the surface mixing layer and bottom boundary layer. No further CTD profiles are available in the vicinity of the measurement site so potential temporal changes in background stratification are not known. The critical internal wave frequency at which the inclination of the group velocity vector matches the bottom slope is given by:

$$\sigma_{cr} = (f^2 \cos^2 \alpha + N^2 \sin^2 \alpha)^{1/2}, \quad (5)$$

where  $f = 1.49\text{ cpd}$  is the local inertial frequency. With  $N$  and  $\alpha$  given above, this yields  $\sigma_{cr} = 2.8 \pm 0.7\text{ cpd}$ . The estimated mean bottom slope is larger than the critical slope for

semidiurnal internal tides  $\alpha_{M_2,cr} = 2.9^\circ \pm 1^\circ$ , but less than the critical slope for the  $M_4$  component  $\alpha_{M_4,cr} = 8.5^\circ \pm 3^\circ$ . Hence, internal  $M_2$  and  $M_4$  tides, both propagating at near critical inclinations, may be favorable for wave-breaking upon reflection at the bottom.

The slope Burger number  $S = N^2 \sin^2 \alpha / f^2 = 2.8 \pm 1.7$ , and characteristics of the observed boundary layer are expected to be significantly different from those above a flat bottom (Garrett, 1990).

### 3. Near-bottom current and temperature observations

At all depths within the measurement range, currents are strongest in the alongslope direction. Maximum values of alongslope, cross-slope and bottom-normal currents are  $u = \pm 0.6 \text{ m s}^{-1}$ ,  $v = \pm 0.25 \text{ m s}^{-1}$ ,  $w = \pm 0.06 \text{ m s}^{-1}$ , respectively (Fig. 3). The variance of the alongslope velocity increases in the lowest 10 m and is roughly constant above that level. Fluctuations of the bottom-normal velocity increase monotonically with distance from the bottom, whereas cross-slope velocity fluctuations decrease slightly with height. The deployment period resolved the spring-neap tidal cycle, which shows a symmetric signal in the alongslope velocity component, but amplified down-slope currents and nearly time-independent maximum up-slope velocities. The alongslope and bottom-normal components are dominated by  $M_2$  fluctuations with upward phase propagation. The cross-slope velocity contains an  $M_4$  component of similar magnitude as its  $M_2$  component (Fig. 4). Similar enhancement of the cross-slope  $M_4$  component has been observed at the continental slope near northwest Africa (Huthnance and Baines, 1982) but also in shallow seas like the North Sea. It might indicate bottom-trapped internal tides (Maas and Zimmerman, 1989b) or reflection of internal semidiurnal tidal waves (Thorpe, 1987a).

The cross-slope flow associated with a reflecting internal wave on a plane slope is expected to be asymmetric, similar to our observations. In this idealized case stronger flows are accompanied by stronger stratification (thinner layers) and weaker counterflows by weaker stratification (thicker layer), so that there is a nonzero Eulerian flow, but no net cross-slope transport (Thorpe, 1987a). Similarly, nonzero Eulerian mean flows may result from topographic steering. However, the observed current and temperature field indicate either internal waves generated at the shelf break and propagating down-slope, or incoming from offshore and reflecting up-slope of the mooring site. The two cases are not distinguishable from our velocity data alone. Observed rapid temperature drops are inconsistent with critical wave reflection (Gemrich and van Haren, 2001) or topographic steering, and it is more likely that our observations reveal internal waves generated at the shelf break and propagating down-slope.

The three-week mean Eulerian current is bottom-trapped. It is oriented down-slope and in the negative alongslope direction (shallow part to the right) with a maximum magnitude of  $9 \times 10^{-2} \text{ m s}^{-1}$  at  $\sim 5 \text{ m}$  above the bottom (Fig. 5). An explanation for this maximum is suggested in Section 5. At the boundary, the bottom-normal velocity has to vanish and nonzero bottom-normal velocities would indicate an incomplete rotation of the coordinate system. We find the mean bottom-normal velocity to be negative at all depths and at our

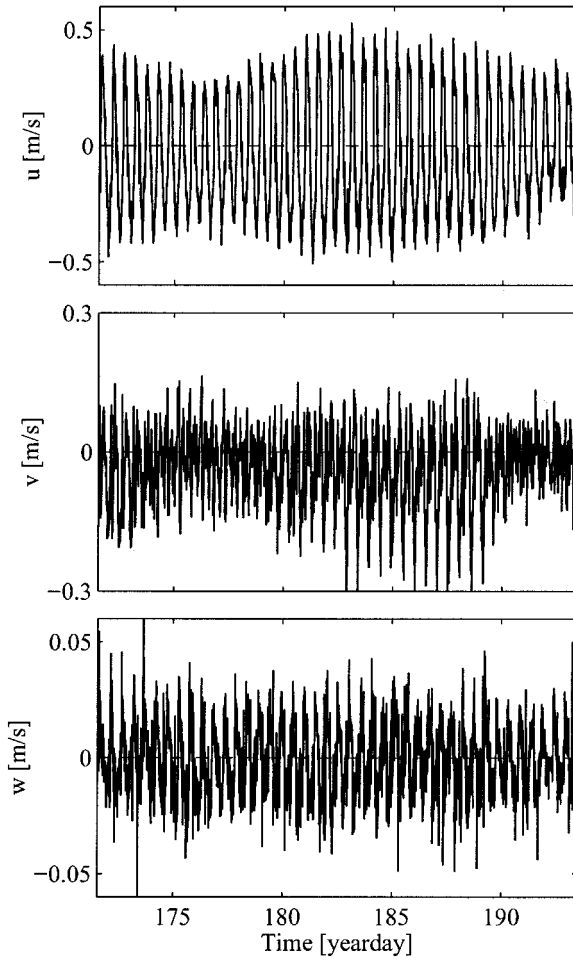


Figure 3. Alongslope  $u$ , cross-slope  $v$  and bottom-normal  $w$  velocity components 13.9 m above the bottom. Note different velocity scales. Time is given in year-days, according to the convention that January 1, 12:00 UTC = 0.5.

lowest measurement bin, 1 m above the bottom,  $|\bar{w}| < 10^{-3} \text{ m s}^{-1}$ . This low value supports our estimate of the bottom slope. Mean currents averaged over four tidal cycles reveal the same shape of the profiles and a spring-neap tide modulation of the layer-averaged current magnitude between  $0.02 \text{ m s}^{-1}$  and  $0.06 \text{ m s}^{-1}$ . This fortnightly mean flow modulation is strongest in the cross-slope direction.

The three-week mean vertical shears for  $u$  and  $v$  are both positive above 4 m. Mean velocities within the range of the downward-looking ADCP are smaller than the velocity in the lowest bin of the upward-looking ADCP, indicating a negative shear at levels below 4 m. In the idealized case of a boundary layer above an infinite homogeneous slope a

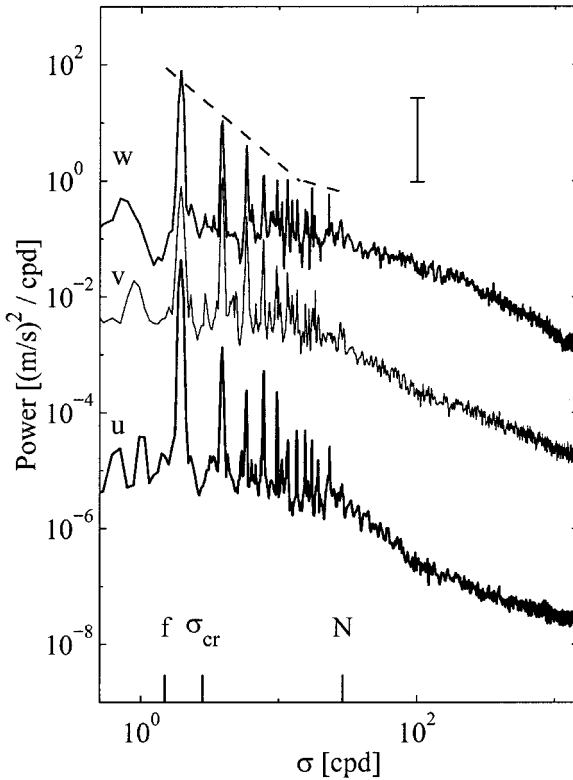


Figure 4. Power spectra computed from velocity records at 13.9 m. Spectra of  $v$  and  $w$  are offset by 3 and 6 decades, respectively. The error bar indicates the 95% confidence interval for the lowest frequencies.  $f$ ,  $N$ ,  $\sigma_{cr}$  mark the local inertial frequency, average buoyancy frequency and the frequency where the wave group velocity vector matches the local bottom slope, respectively. Dashed lines depict slopes  $\sigma^{-n}$ ,  $n = 2$  (left) and  $n = 0.7$  (right).

buoyancy-driven secondary circulation is expected (Phillips *et al.*, 1986). The predicted steady-state alongslope flow is negative within the boundary layer and positive outside. The steady-state cross-slope current has a bidirectional structure with positive near-bottom values (Garrett, 1990); however, the solution to the unsteady problem of flow formation along an inclined plane yields no sign reversal of the cross-slope flow (Kistovich and Chashechkin, 1993). The observed profile of the alongslope flow would only be consistent with the predicted steady-state secondary flow for a boundary-layer thickness  $>45$  m. However, no mean up-slope current in the near-bottom layer is observed.

Associated with the  $M_2$  velocity fluctuations are temperature fluctuations which reach magnitudes  $>2$  K during spring tide (Fig. 6a). It is likely that these temperature fluctuations are caused by advection of cross-slope temperature gradients by internal waves, where the up-slope motion carries colder water from deeper levels up the slope and the down-slope flow advects warmer water from higher up the slope. For a uniform bottom

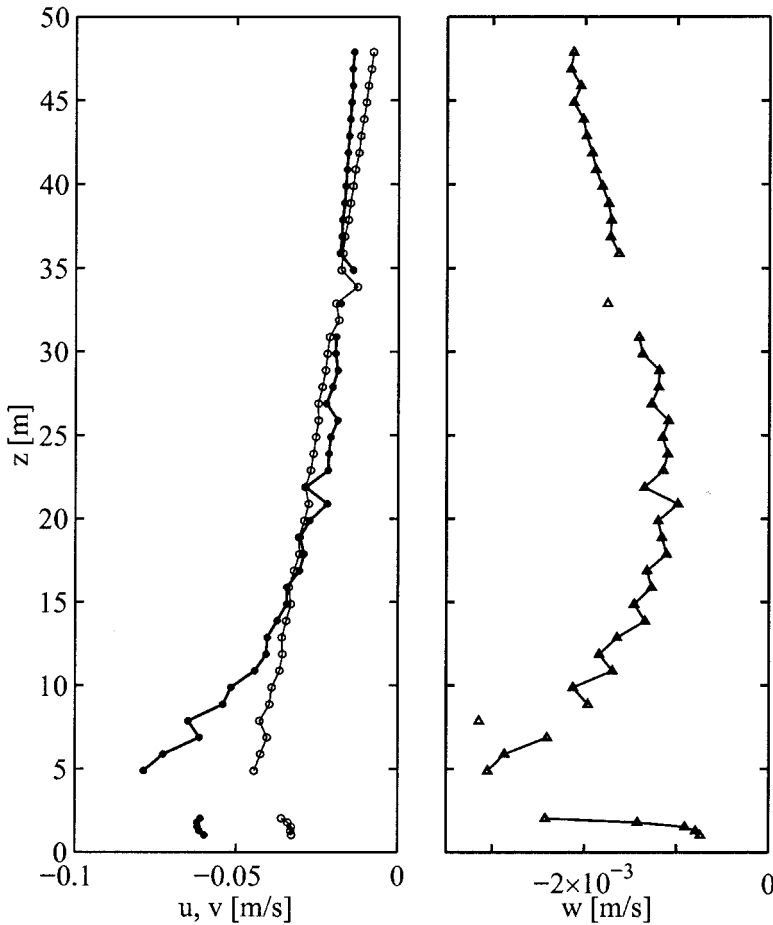


Figure 5. Three-week mean velocity profiles. Left: Alongslope component  $u$  (filled circles) and cross-slope component  $v$  (open circles). Right: Bottom-normal component  $w$  (triangles). Note different scales. One standard deviation is  $3 \times 10^{-5} \text{ m s}^{-1}$  for  $u$ ,  $v$  and  $1 \times 10^{-5} \text{ m s}^{-1}$  for  $w$ .

slope with a constant cross-slope temperature gradient, symmetric temperature fluctuations are expected. However, the observed temperature fluctuations are asymmetric with larger negative fluctuations, which are not consistent with the observed amplified down-slope current. Internal waves propagating obliquely down-slope may advect colder (denser) water higher on the slope than lighter (warmer) fluid, resulting in a gravitationally unstable cross-slope stratification (Gemrich and van Haren, 2001). The collapse of this stratification will restrain the advection of warmer water, similar to our observations. However, the observed asymmetric behavior of the observed temperature fluctuations may also be associated with shallower bottom slopes, and therefore weaker cross-slope temperature gradients, up-slope of the deployment site. Although the temperature record resembles the

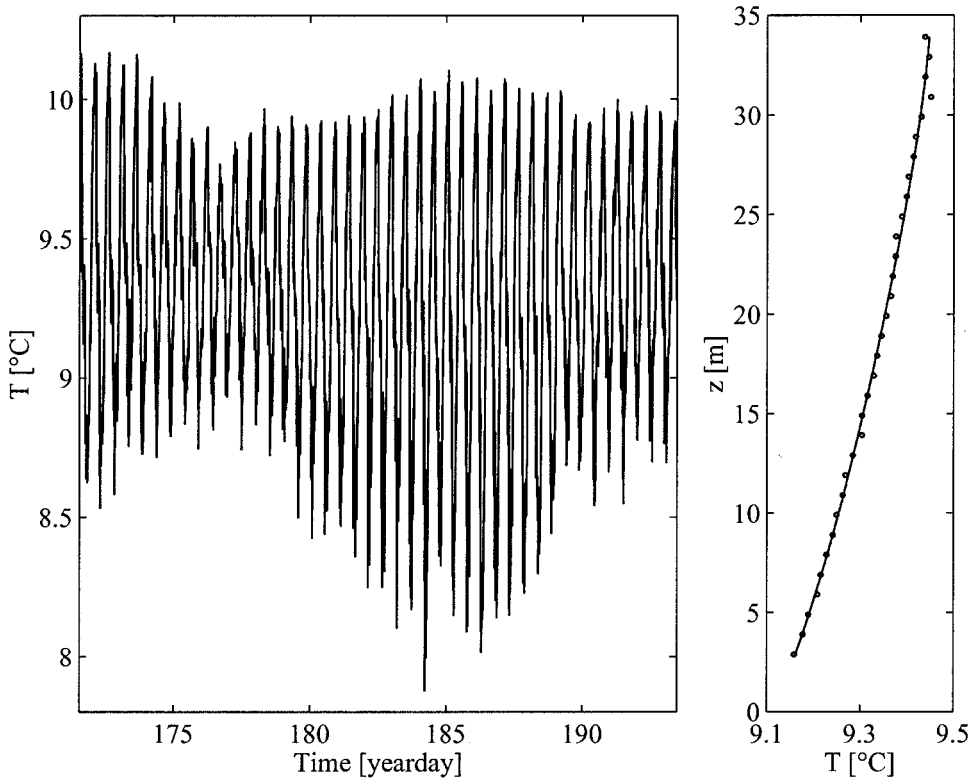


Figure 6. Left: Temperature record observed at 13.9 m above the bottom. Right: three-week mean temperature profile. Measured temperature adjusted by thermistor calibration offsets (dots) and third order polynomial fit (line) are shown.

asymmetric temperature fluctuations associated with internal wave reflection and associated nonlinear resonance (Thorpe, 1987a, 1992, 1999; Slinn and Riley, 1996) the observed velocity field is not consistent with this scenario.

The three-week mean temperature profile shows stable near-bottom stratification (Fig. 6b). Mean temperature gradients are  $12 \times 10^{-3} \text{ K m}^{-1}$  between 2.9 m and 14.9 m and  $7 \times 10^{-3} \text{ K m}^{-1}$  in the layer 14.9 m–33.9 m. Previous observations over sloping bottom boundaries indicated the existence of a well-mixed layer (Armi and Millard, 1976) or stratification with temperature gradients two orders of magnitude smaller than found in our data set (Thorpe, 1987b). Toole *et al.* (1997) observed significant stratification in the near-bottom region above the flank of a seamount. At our deployment site, there is considerable variability in the thermal stratification with  $M_2$  periodicity (Fig. 7), alternating between periods of weak and strong stratification. Strongly stratified periods occur roughly between times of maximum and minimum alongslope velocity when vertically-averaged temperature gradients reach up to  $4 \times 10^{-2} \text{ K m}^{-1}$ . Periods of weak stratification

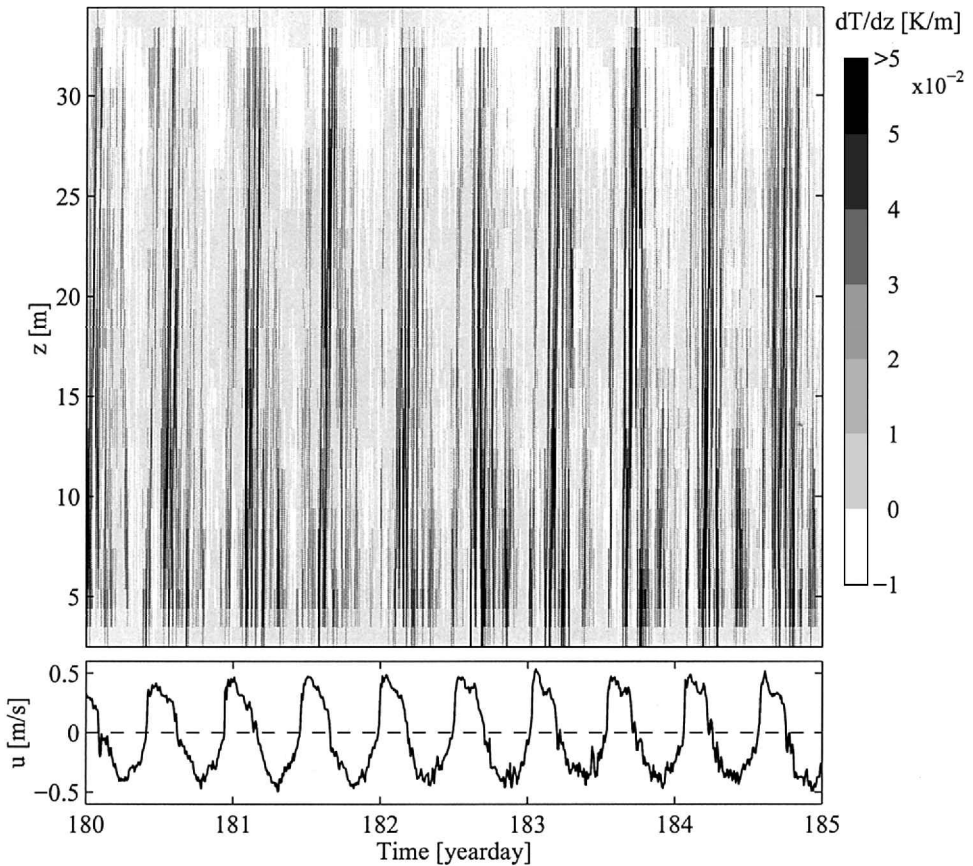


Figure 7. Five days of vertical temperature gradient obtained from offset-adjusted thermistor string record. Lower panel shows alongslope velocity at 13.9 m.

are centered around the time when the alongslope current reverses from negative to positive values, associated with thermal fronts (Gemrich and van Haren, 2001).

The mean temperature profile provides an estimate of the mean local buoyancy profile  $\overline{B(z)} = -g(\overline{\rho(z)} - \rho_0)/\rho_0$ , where  $\overline{\rho}$  is the mean density and  $\rho_0$  is the density of a reference fluid, which satisfies the hydrostatic equilibrium. Assuming that the tight T-S relationship obtained from the CTD profile at the beginning of the experiment is valid throughout the deployment period, the buoyancy may be estimated as  $\overline{B(z)} = -g\gamma(\overline{T(z)} - T_0)/\rho_0$  with  $\gamma = 0.184 \text{ kg m}^{-3} \text{ K}^{-1}$ . The reference temperature  $T_0$  is taken as the three-week mean temperature at our lowest thermistor and the reference density  $\rho_0$  is specified by  $T_0$  and salinity given in the CTD profile at 830 m depth. The mean temperature varies by 0.3 K over the range of the thermistor string (Fig. 6b). Thus, the buoyancy increases by  $\sim 5 \times 10^{-4} \text{ m s}^{-2}$  over this range. However, some variability in the

T-S relationship throughout the deployment period is likely and the above stated buoyancy can only be considered a first estimate.

#### 4. Internal wave band fluxes

The focus of this study is to evaluate vertical fluxes of heat and momentum supported by the internal wave band. Flux contributions within this frequency band are due to nonlinear (breaking) internal waves and turbulence. Estimates of eddy fluxes require a spectral gap separating mean and fluctuating parts of velocities and temperature. An obvious choice for the cut-off frequency  $\sigma_c$  is at the lower bound of the internal wave band. However, above a sloping boundary, the energy density of near-critical internal waves increases, destabilizing waves of higher frequencies. Therefore, we expect that within the internal wave band, mainly internal waves with frequencies higher than the critical frequency are prone to breaking and contribute to diapycnal mixing. We are interested in the effects these high-frequency waves may have on the low-frequency flow. A spectral gap yielding an obvious separation between high- and low-frequency internal waves is not apparent in our data (Fig. 4). The velocity spectra fall off as  $\sigma^{-n}$ , where  $n = 2$  is the canonical value in the internal wave band. For the observed velocity components the value of  $n$  changes from  $n \geq 2$  to  $n \approx 0.7$  at  $\sigma \approx 15$  cpd (Fig. 4). This shift of spectral characteristics is utilized to define the high-frequency internal waves by applying a cut-off frequency  $\sigma_c = 15$  cpd. Additionally, the relevance of mean flow modification by low-frequency internal waves, dominated by the internal tide, will be examined using a cut-off frequency  $\sigma_c = 1.9$  cpd.

In practice, mean and fluctuating parts were separated with a third order high-pass elliptic filter, applied in forward and reverse direction in order to eliminate phase shifts. This filter assured that for the cut-off frequency of 1.9 cpd the semidiurnal tidal signal is fully included in the fluctuating part of the signal. The same filters were applied for the velocities and temperature records. No high-frequency pre-filtering has been applied and the obtained fluxes cover the specified internal wave band, including large turbulence scales up to the Nyquist frequency, well beyond  $N$ . However, small-scale turbulence and dissipation scales are not resolved with our instrumentation.

First, we consider bottom-normal eddy fluxes supported by the high-frequency part of the internal wave band. In alongslope as well as cross-slope direction, fluxes of horizontal momentum are highly variable (Fig. 8). For short periods, fluxes exceed the mean values by more than one order of magnitude. These events are most frequent during spring tide, occurring at irregular intervals up to five times per day. The vertical extent of intense fluxes is, in most cases, limited to  $\sim 5\text{--}25$  m with its center at variable heights above the bottom (Fig. 9). In the alongslope direction, fluxes  $\overline{u'w'}$  are mainly positive, whereas cross-slope fluxes  $\overline{v'w'}$  are mainly negative. The magnitude of the peaks is  $O(10^{-3} \text{ m}^2 \text{ s}^{-2})$  and is slightly smaller for the cross-slope than the alongslope component. During current maxima, bottom induced shear stresses  $C_D \mu^2$  can be of similar magnitude, assuming a drag coefficient  $C_D = 2.5 \times 10^{-3}$ . However, maxima in the observed momentum fluxes do not coincide with current maxima and therefore are not associated with bottom friction.

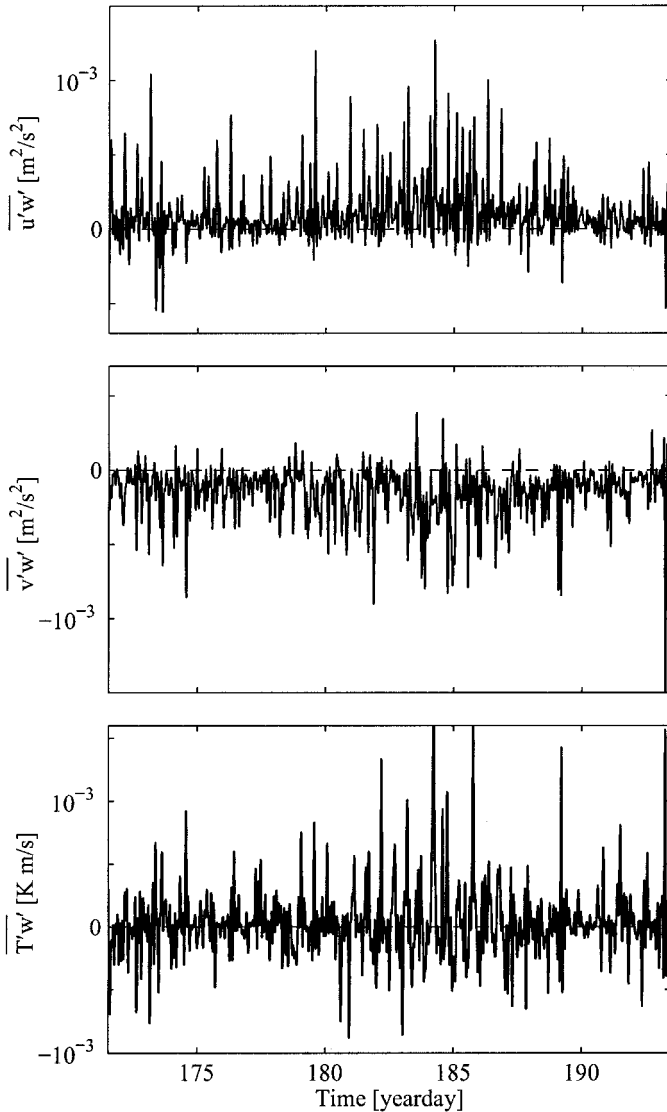


Figure 8. Vertical fluxes of horizontal momentum and heat from observations at 13.9 m above the bottom. The Reynolds decomposition cut-off is  $\sigma_c = 15$  cpd. (a) Flux of alongslope momentum, (b) flux of cross-slope momentum, and (c) heat flux.

Individual internal waves support a vertical flux of horizontal momentum, except at frequencies  $f$  and  $N$ . In an isotropic wave field, e.g. generated by wave reflection, the combined fluxes of waves with upward and downward energy propagation cancel out. We observe intense momentum fluxes, mainly limited to a small vertical range. These occurrences of significant momentum fluxes imply anisotropy in the internal wave field or

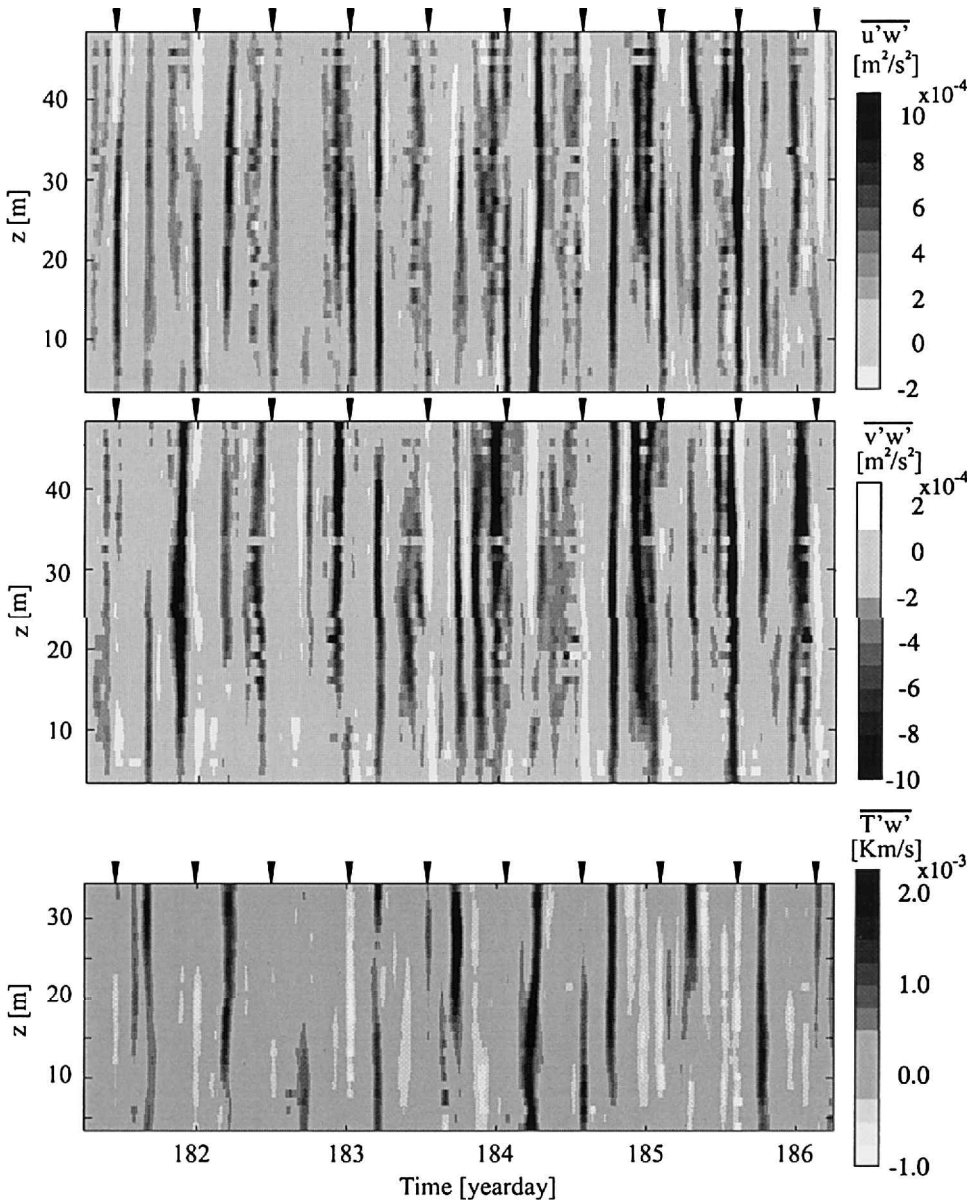


Figure 9. Five days of space-time distribution of vertical fluxes ( $\sigma_c = 15$  cpd) of (a) alongslope momentum, (b) cross-slope momentum, and (c) heat. For clarity, small fluxes are clipped to zero (see color bars). Arrowheads indicate times of current reversal from negative to positive alongslope current. Note the thermistor string data logger interfered with current observations near 32 m, due to first side-lobe contamination.

local instabilities. Strong momentum fluxes during reversals from negative to positive alongslope current are most likely linked to the collapse of unstable stratification. As mentioned in Section 3, internal waves propagating obliquely to the sloping bottom may generate unstable cross-slope stratification. For the observed current field this unstable stratification reaches a maximum at the reversal from negative to positive alongslope current (Gemrich and van Haren, 2001). The resulting strong momentum fluxes occur regularly and are most pronounced in the bottom  $\sim 30$  m (Fig. 9).

Heat fluxes associated with high-frequency internal waves are rapidly alternating between positive (upward) and negative (downward) values, and magnitudes  $>3 \times 10^{-3} \text{ K m s}^{-1}$  (i.e. equivalent buoyancy flux  $O(5 \times 10^{-6} \text{ W k g}^{-1})$ ) are common in our observations (Fig. 8c). For purely linear waves, velocities and temperature fluctuations are phase-shifted by  $\pi/2$  and fluctuating, and no mean heat flux is supported. Therefore, periods of significant heat fluxes imply mixing events, possibly associated with breaking internal waves. Such mixing events occur regularly in the near-bottom layer (Fig. 9). There are several events with strong momentum fluxes lacking a corresponding heat flux. These events are caused by anisotropy in the internal wave field, which does not require diapycnal mixing.

Three-week mean momentum fluxes for high-frequency internal waves as well as those for the entire internal wave band are positive in alongslope direction and bottom-normal direction and negative in the cross-slope direction (Fig. 10). All mean momentum flux values are significantly different from zero at the 95% level. A flux estimate is considered to be statistically significantly different from zero if it falls outside the confidence interval of the distribution of the lagged covariance of the two fluctuating quantities. The basis of this method of determining statistical significance of our flux estimates has been suggested by Ruddick (pers. comm., 1990), and described earlier (Yamazaki and Osborn, 1993; Fleury and Lueck, 1994; van Haren *et al.*, 1994). We used a computationally faster way suggested by Lueck and Wolk (1999), for appropriate flux estimates using ADCP and thermistor string data (van Haren, 2000). In the alongslope direction, only  $<8\%$  of the total momentum flux is supported by high-frequency waves and  $>80\%$  by the internal tide. The magnitude of momentum fluxes supported by high-frequency waves is almost equal for all three components. However, contributions by lower frequency internal waves are much less in cross-slope and bottom-normal directions, suggesting a strong anisotropy of low-frequency internal waves.

Only three-week mean heat fluxes associated with high-frequency internal waves ( $\sigma \geq 15$  cpd) are significantly different from zero (Fig. 11). The strongest flux occurs in the alongslope direction, where the fluxes exceed  $2 \times 10^{-4} \text{ K m s}^{-1}$ . Bottom-normal fluxes are positive (upward), and thus counter-gradient. The maximum bottom-normal heat flux value is  $8 \times 10^{-5} \text{ K m s}^{-1}$ . In the range 7–12 m, estimates of this heat flux are not significantly different from zero. In the cross-slope direction high-frequency heat fluxes are positive (up-slope) near the bottom and down-slope for  $z > \sim 12$  m.

Heat fluxes associated with the semidiurnal tidal frequency are up to two orders of

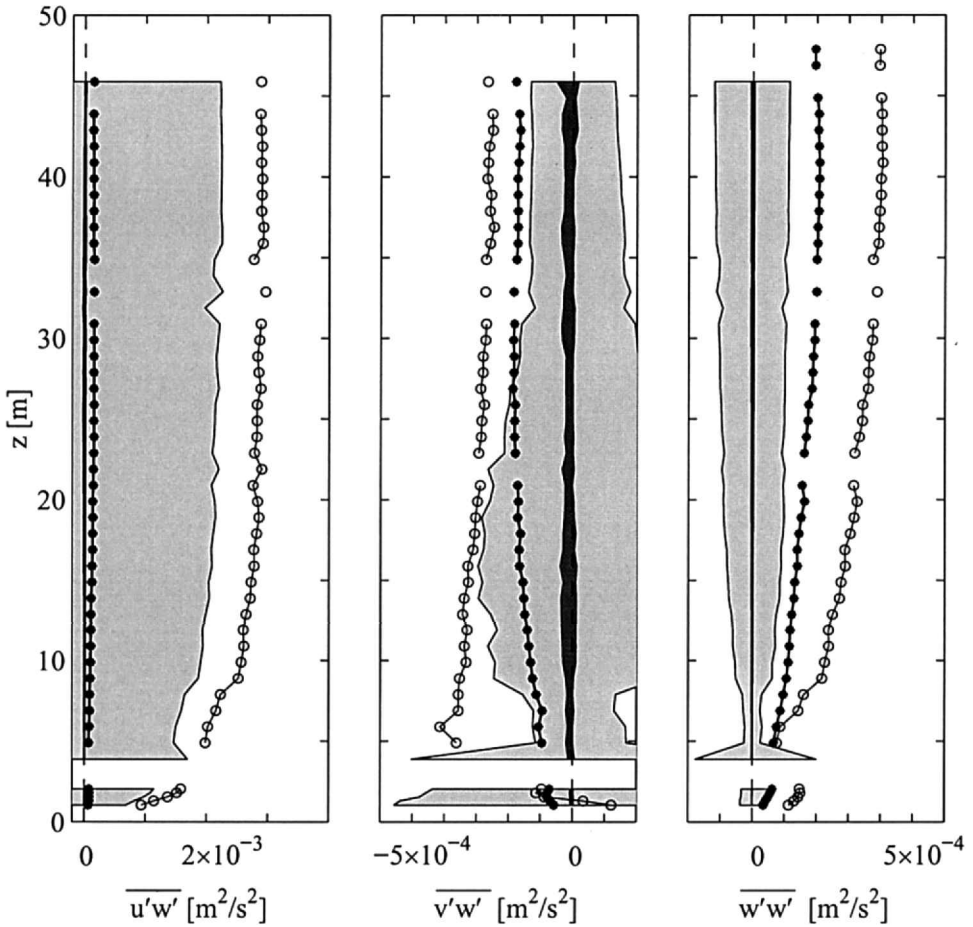


Figure 10. Mean profiles of Reynolds stress components of complete deployment period, for high-frequency internal waves,  $\sigma \geq 15$  cpd (solid circles), and wave band including the internal tide,  $\sigma \geq 1.9$  cpd (open circles). Flux estimates outside the shaded areas (dark shading for  $\sigma \geq 15$  cpd, light shading  $\sigma \geq 1.9$  cpd) are significantly different from zero at the 95% confidence level. Left: Alongslope direction. Center: cross-slope direction. Right: Bottom normal component. Note the different scales of the horizontal axes.

magnitude larger than fluxes supported by high-frequency fluctuations (Fig. 11). However, the low-frequency ( $\sigma \geq 1.9$  cpd) related heat fluxes are not statistically significant. For a cut-off frequency of 3 cpd, thereby excluding the flux contributions by the semidiurnal tide, the obtained heat flux components are also non-significant throughout the monitoring range.

As stated above, the fluxes consist of contributions from internal waves and large-scale turbulence. Linear waves yield zero mean flux and large bounds of the 95% significance test. Therefore, nonzero mean heat fluxes which are considerably different from the

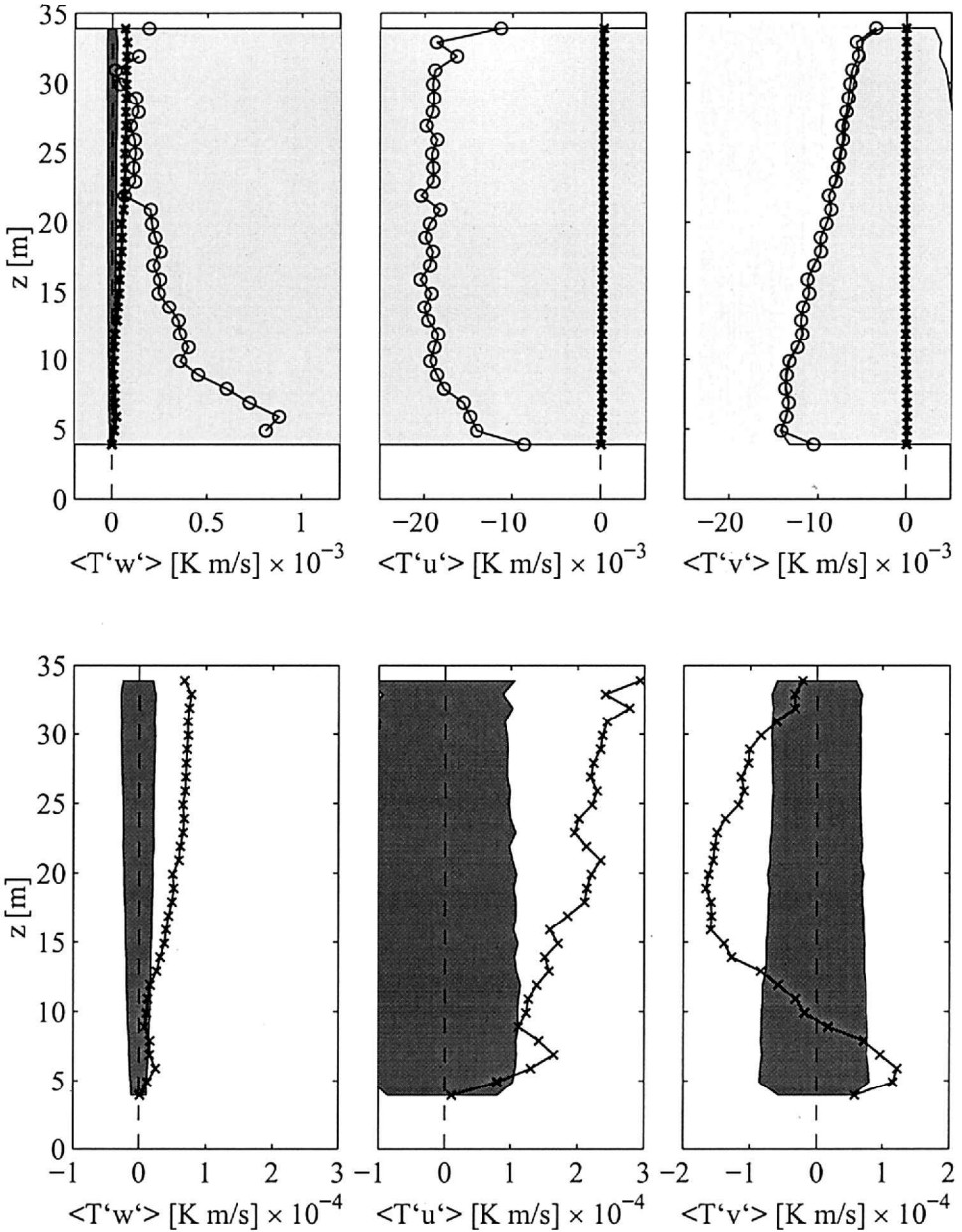


Figure 11. Three-week mean vertical heat flux profiles (bottom-normal  $\langle T'w' \rangle$ , alongslope  $\langle T'u' \rangle$  and cross-slope  $\langle T'v' \rangle$ ). Top: Flux profiles for high-frequency internal waves,  $\sigma \geq 15$  cpd (crosses), and wave band including the internal tide,  $\sigma \geq 1.9$  cpd (open circles). Flux estimates outside the shaded areas (dark shading for  $\sigma \geq 15$  cpd, light shading  $\sigma \geq 1.9$  cpd) are significantly different from zero at the 95% confidence level. Bottom: For  $\sigma \geq 15$  cpd. (Note different scales.)

significance bounds imply the presence of nonlinear waves. We find that mainly the high-frequency waves are nonlinear.

## 5. Discussion

The dynamics of the boundary layer above an infinite slope without alongslope variations can be described by simplified momentum and heat equations (e.g. Garrett, 1991):

$$\overline{\frac{\partial u}{\partial t}} - \overline{fv} = \frac{\partial \tau_x}{\partial z} \quad (6)$$

$$\frac{\partial v}{\partial t} + \overline{fu} = \frac{\partial \tau_y}{\partial z} + \overline{B} \sin \alpha - \frac{1}{\rho_0} \frac{\partial \overline{p}}{\partial y} \quad (7)$$

$$0 = \frac{\partial \tau_z}{\partial z} + \overline{B} \cos \alpha - \frac{1}{\rho_0} \frac{\partial \overline{p}}{\partial z} \quad (8)$$

$$\frac{\partial T}{\partial t} + \overline{u} \frac{\partial T}{\partial x} + \overline{v} \frac{\partial T}{\partial y} + \overline{w} \frac{\partial T}{\partial z} = - \frac{\partial}{\partial z} \overline{T'w'} \quad (9)$$

where the overbar denotes a suitable mean,  $B$  is the local buoyancy, and  $p$  is the pressure minus the hydrostatic pressure of the reference fluid. We assume for the vertical components of stress divergence

$$\frac{\partial \tau_x}{\partial z} = - \frac{\partial}{\partial z} \overline{u'w'}, \quad \frac{\partial \tau_y}{\partial z} = - \frac{\partial}{\partial z} \overline{v'w'}, \quad \text{and} \quad \frac{\partial \tau_z}{\partial z} = - \frac{\partial}{\partial z} \overline{w'w'}. \quad (10)$$

The theoretical framework (6)–(9) can only be considered a first estimate. The idealization of an infinite uniform slope is a crude description of the given situation. For nonuniform slope conditions, cross-slope and alongslope flux divergences may exist and may be dynamically relevant.

Our observations do not allow evaluation of terms in (6)–(9) involving alongslope and cross-slope gradients or pressure. However, we estimate the relative significance of bottom-normal momentum and heat-flux divergences for the dynamics of the sloping boundary layer, which is possible from our data set. Moreover, evaluation of the resolvable terms yields an indirect evaluation of the terms which cannot be resolved from our observations. For the following discussion, we will consider a steady state and evaluate the quantifiable terms in (6)–(9) for the three-week means.

The alongslope momentum equation (6) describes the classical Ekman flow. However, we find the Coriolis term does not balance the momentum-flux divergence (Fig. 12a). The momentum-flux divergence associated with the internal tide dominates the alongslope momentum, especially at  $z < \sim 18$  m. This strong near-bottom flux divergence indicates that additional processes dominate the dynamics in this layer. Possible unresolved terms

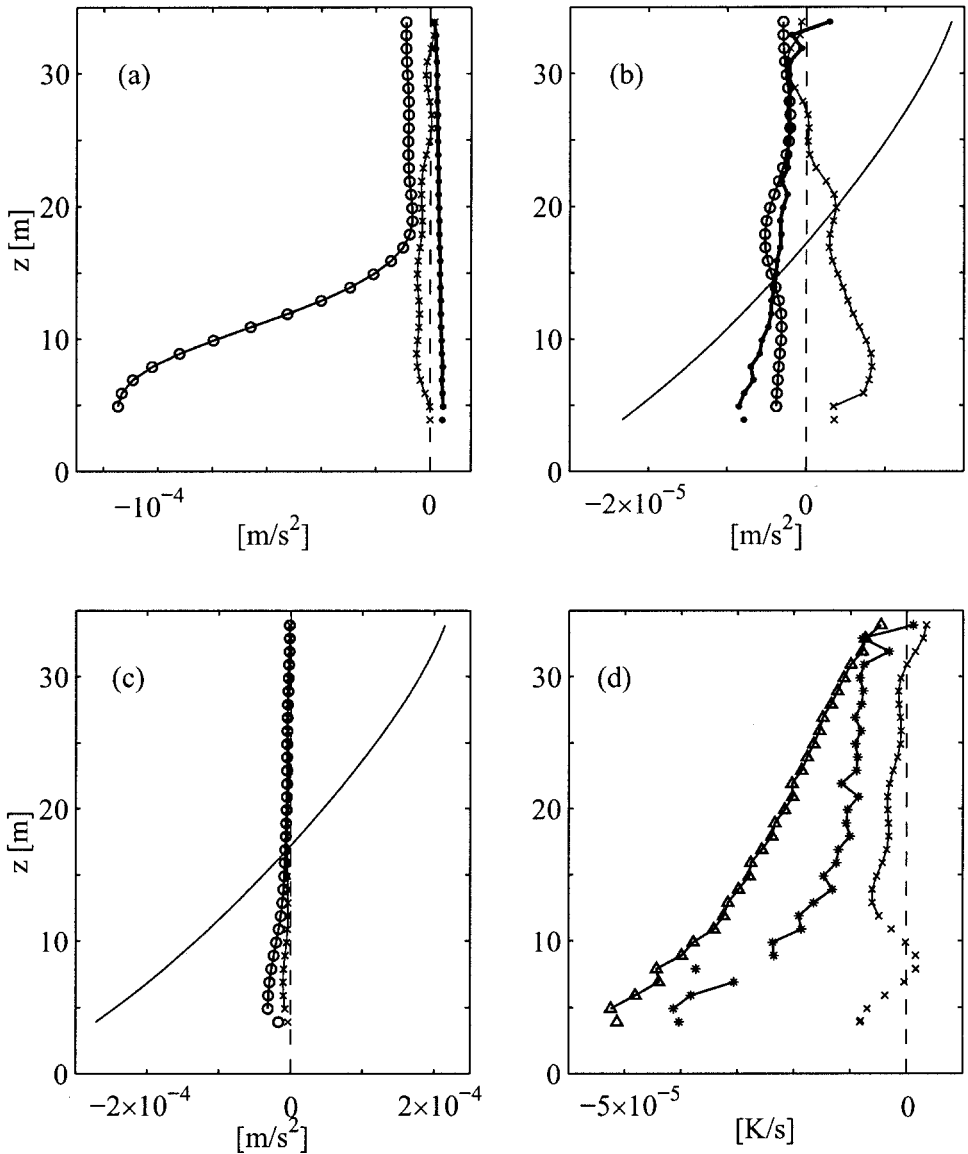


Figure 12. Three-week average estimates of terms describing the mean flow and buoyancy above an idealized slope (see text). (a) Alongslope momentum,  $-\bar{f}v$  (thick solid line),  $-\partial/\partial z(\overline{u'w'})$  (circles:  $\sigma_c = 1.9$  cpd, crosses:  $\sigma_c = 15$  cpd). (b) Cross-slope momentum,  $\bar{f}u$  (thick solid line),  $-\partial/\partial z(\overline{v'w'})$  (circles:  $\sigma_c = 1.9$  cpd, crosses:  $\sigma_c = 15$  cpd),  $\bar{B} \sin \alpha + C$  (thin solid line). (c) Bottom-normal momentum  $-\partial/\partial z(\overline{w'w'})$  (circles:  $\sigma_c = 1.9$  cpd, crosses:  $\sigma_c = 15$  cpd),  $\bar{B} \cos \alpha + C_2$  (thin solid line). (d) Heat equation,  $\bar{v}\partial\bar{T}/\partial y$  (triangles),  $\bar{w}\partial\bar{T}/\partial z$  (asterisks), and  $-\partial/\partial z(\overline{T'w'})$  (crosses,  $\sigma_c = 15$  cpd). For clarity, buoyancy terms are offset by unspecified constants  $C$  and  $C_2$ .

include alongslope and cross-slope flux divergences or a density related alongslope pressure gradient. It may even be that bottom friction associated with the internal tide generates a turbulent boundary layer. For a baroclinic tidal flow over topography, Maas and Zimmerman (1989a,b) predict a negative and bottom-intensified mean alongslope current. This is entirely consistent with our observations. A momentum-flux divergence associated with the turbulent boundary layer would be bottom-intensified and positive, as is required to balance the alongslope momentum (6).

In the cross-slope direction (7), all quantifiable terms are of similar magnitude (Fig. 12b). Above  $z \sim 20$  m, the Ekman balance is valid for total internal wave band stress divergence. Buoyancy estimates are an order of magnitude larger than Coriolis force or momentum-flux divergences, suggesting two superimposed regimes. The Ekman balance is related to the internal tide, whereas a potential imbalance between buoyancy term and pressure-gradient term could result in the secondary circulation predicted above a sloping bottom. Unfortunately, our data do not allow us to test this hypothesis. At  $z < \sim 25$  m, momentum flux divergences associated with high-frequency internal waves are opposite to those associated with the internal tide. This points to momentum being transferred from the internal tide to higher frequencies as well as to the mean flow.

A lower bound of the variations in magnitude of the buoyancy term in the bottom-normal momentum equation (8) is  $5 \times 10^{-4} \text{ m s}^{-2}$ . Momentum-flux divergences are at least one order of magnitude smaller (Fig. 12c), again suggesting a balance between buoyancy term and the unknown pressure-gradient term. The momentum-flux divergences, which decrease from  $3 \times 10^{-5} \text{ m s}^{-2}$  ( $\sigma \geq 1.9$  cpd), and  $1 \times 10^{-5} \text{ m s}^{-2}$  ( $\sigma \geq 15$  cpd) in the lowest profiling bin to a frequency independent value of  $4 \times 10^{-7} \text{ m s}^{-2}$  above 35 m, may support a (weak) residual circulation.

Over a slope, nonlinear tidal advection may generate a three-cell residual circulation in a vertical plane normal to the isobaths (Maas and Zimmerman, 1989b). The strongest currents occur in the center of the circulation, where negative alongslope current combined with a down-slope flow are predicted. Down-slope as well as alongslope currents are bottom-intensified. Our observed three-week mean alongslope, cross-slope and bottom-normal currents are consistent with the predicted circulation. A similar structure of the mean flow has been observed above a slope in the much shallower, stratified North Sea (van Haren, 1990). However, here we do not have sufficient information to test this hypothesis.

The high-frequency heat-flux divergence in (9) is greatest for  $z < \sim 25$  m with an average value of  $5 \times 10^{-6} \text{ K s}^{-1}$  (Fig. 12d). For  $z > 25$  m the flux-divergence averages to  $10^{-6} \text{ K s}^{-1}$ . The observed positive divergence of the heat flux should cause cooling of the near-bottom layer by  $\sim 9$  K during the deployment period. Since the temperature record (Fig. 6a) shows no general trend, the cooling associated with flux-divergence must be balanced by heat advection or (alongslope and cross-slope) divergence of alongslope or cross-slope heat fluxes. Heat fluxes supported by low-frequency internal waves are

insignificant and, therefore, low-frequency bottom-normal heat flux divergence is not considered, although they do have proper magnitudes for balance.

In theory, bottom-normal heat advection vanishes close to the bottom under the assumption of an infinite slope without alongslope variation (Garrett, 1991). In an experimental study of boundary-layer dynamics Trowbridge and Lentz (1998) assumed this term to be negligible. Here, the bottom-normal heat advection, estimated as the product of the mean bottom-normal velocity and the mean bottom-normal temperature gradient, yields approximately  $-10^{-5} \text{ K s}^{-1}$ , with larger magnitudes for  $z < \sim 15 \text{ m}$ . Hence, similar to van Haren *et al.* (1994), but at values one decade larger, we find the neglect of bottom-normal heat advection is not justified for our observations.

Alongslope and cross-slope temperature gradients are not directly measured and can only be estimated. Temperature gradients of order  $5 \times 10^{-4} \text{ K m}^{-1}$  are required for the alongslope or cross-slope advection terms to be as important as bottom-normal advection or flux divergence. At least in the cross-slope direction, it is likely to find such temperature gradients. In the idealized case of horizontal (normal to gravity) isotherms, the cross-slope temperature gradient is estimated by  $\partial T/\partial y = \sin \alpha \partial T/\partial z$ , yielding  $\partial T/\partial y \approx 5 \times 10^{-4} \text{ K m}^{-1}$  and a cross-slope heat advection of  $-10^{-5} \text{ K s}^{-1}$ , i.e. a down-slope transport of warmer water-masses. However, uncertainties of this temperature gradient estimate may be large and it can only be concluded that bottom-normal heat-flux divergence plays a less important role compared to heat advection.

In the concept of eddy exchange coefficients, fluxes are parameterized in terms of the three-week mean gradients by

$$\overline{u'w'} = -A_x \frac{\overline{\partial u}}{\partial z}, \quad \overline{v'w'} = -A_y \frac{\overline{\partial v}}{\partial z}, \quad \overline{T'w'} = -K \frac{\overline{\partial T}}{\partial z}, \quad (11)$$

where  $A_x$ ,  $A_y$  are eddy viscosities obtained for alongslope and cross-slope directions, respectively, and  $K$  is the eddy diffusivity. Here, the fluxes represent the contribution by the internal wave band and, therefore, the eddy viscosities and eddy diffusivity are not necessarily the same as the eddy exchange coefficients associated with true turbulence.

Between  $z = 1 \text{ m}$  and  $z = 2 \text{ m}$ , mean shear values are negative, for  $z > 5 \text{ m}$  they are generally positive. At all levels, mean momentum fluxes are positive alongslope and negative across-slope, independent of the cut-off frequency considered. Only high-frequency internal waves show nonlinearities and significant buoyancy fluxes. Therefore, we will consider only a decomposition using a cut-off  $\sigma_c = 15 \text{ cpd}$  in the following discussion.

Eddy viscosities in the alongslope and cross-slope directions have opposite signs, independent of distance to the bottom (Fig. 13). Close to the bottom, the alongslope shear is positive. For  $z > 5 \text{ m}$ , positive eddy viscosities are obtained for the cross-slope direction and negative eddy viscosities for the alongslope direction. This implies a momentum transfer from the internal wave band to the mean alongslope current and opposite in the

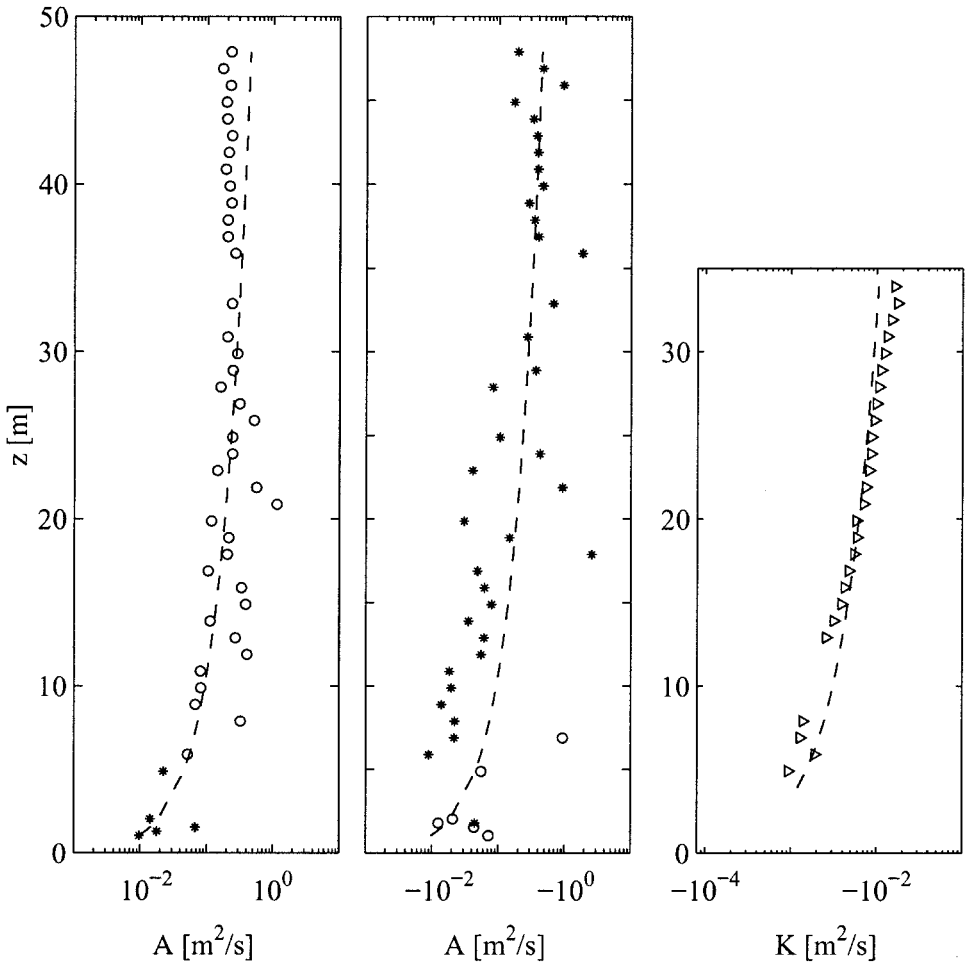


Figure 13. Profiles of three-week mean eddy viscosity  $A$  obtained for alongslope direction (asterisks) and cross-slope direction (circles) and eddy diffusivity  $K$  (triangles), from fluxes with  $\sigma_c = 15$  cpd. Dashed lines depict linear  $z$ -dependence. Note, middle and right panel show negative values!

cross-slope direction. We find the concept of flux parameterization in terms of eddy viscosities is not applicable for the internal wave band.

Eddy diffusivities are negative throughout the monitoring range (Fig. 13c). In the concept of eddy exchange coefficients this is interpreted as processes within the internal wave band restratifying the water column. Since local temperature does not vary much over the course of the measurements, vertical flux divergence yielding negative eddy diffusivities is counteracted by advection or flux divergence in non-bottom-normal direction, as suggested before. Again, the eddy diffusivity concept seems not be appropriate to parameterize internal wave band fluxes in our observations.

The three-week mean eddy Prandtl number  $Pr_t = A/K$  of the bottom boundary layer is  $Pr_t \approx 20$  in the alongslope direction and  $Pr_t \approx -20$  in the cross-slope direction. As linear internal waves do not contribute to the heat flux, the eddy Prandtl number is expected to become infinitely large. The rather small observed value of  $|Pr_t| \approx 20$  indicates a significant buoyancy flux contribution by nonlinear waves and possibly by unresolved turbulence within the internal wave band.

The height of a distinct, weakly stratified boundary layer is not apparent in the three-week mean current or temperature profiles. However, our data indicate that the monitored layer can be divided into two sublayers, with different processes dominating the dynamics. Strong alongslope shear and momentum-flux divergences are confined to  $z < 20$  m. For  $z > 25$  m shear values are an order of magnitude smaller than in the lower layer and momentum fluxes are nearly constant in the vertical. Coriolis force, and possibly pressure gradients and buoyancy forces dominate the dynamics in this layer. Therefore, we infer the mean mixing-layer height  $h = 20$  m. The buoyancy boundary (or “mixed”) layer height above a sloping bottom is  $\delta = \delta_E(1 + SPr_t)^{-1/4}$  (Thorpe, 1987b), where  $\delta_E = \sqrt{2A/f}$  is the Ekman-layer height above a flat bottom. Taking the magnitude of the Prandtl number above and the slope Burger number  $S = 2.8$ , we find  $\delta < 10$  m. Thus,  $\delta < h$  and bottom boundary-layer mixing is expected to be effective (Garrett, 1990). A negative eddy diffusivity implies restratification throughout the bottom boundary layer, i.e.  $\delta \rightarrow 0$ . Processes associated with the high-frequency part of the internal wave-band restratify the near-bottom-layer on which higher frequency turbulent mixing can act, indicating a high mixing efficiency. The upslope flow associated with the secondary circulation is confined to  $z < \delta$  (Garrett, 1990) and therefore not present in our current profile (Fig. 5).

## 6. Conclusions

We have presented results of an observational study of the near-bottom layer up to 45 m above the continental slope in the Bay of Biscay. Our main conclusions are as follows.

- The near-bottom layer is very energetic with currents up to  $0.6 \text{ m s}^{-1}$ . Currents, temperature distribution and stratification are highly variable with time.
- The high-frequency internal wave band supports significant Reynolds stresses and a significant heat flux for  $z > \sim 12$  m. Thus, high-frequency internal waves are anisotropic and nonlinear in our observations in the near-bottom layer.
- The three-week mean alongslope and cross-slope currents are bottom-intensified and down-welling favorable, in Ekman sense. However, the classical Ekman balance does not describe the dynamics of the sloping bottom boundary layer. Momentum-flux divergence of the internal tide dominates the alongslope momentum equation and causes momentum transfer from the tidal frequency to the mean alongslope flow. Buoyancy and pressure gradient forces, which we could not determine directly, may generate a buoyancy-driven secondary flow.
- The temperature distribution is likely dominated by all three components of heat advection with smaller contribution by divergence of the bottom-normal heat flux.

- Processes associated with the high-frequency part of the internal wave-band play an important role in stratifying the near-bottom layer. The internal tide does not contribute to the bottom-normal heat flux significantly. The concept of parameterizing internal wave band fluxes by mean flow gradients is not appropriate.
- Below 25 m, momentum is transferred from the internal tide to higher internal wave frequencies as well as to the mean flow.
- The height of the mixing-layer  $h \sim 20$  m is larger than the height of the mixed-layer  $\delta \rightarrow 0$ . Therefore, any upslope current of the secondary circulations, which is predicted in the lower part of the boundary layer  $z < \delta$ , is below our measurement range, consistent with our observations.
- We expect that the observed mean restratification near the bottom and well within the mixing-layer yields a high mixing efficiency. The assumption that turbulence stirs already mixed water in a sloping near-bottom layer, yielding low mixing efficiency, is not valid in this oceanic observation.

*Acknowledgments.* The data were acquired during the Bay of Biscay Boundary (TripleB) project. We acknowledge the cooperative attitude of Hendrik van Aken for allowing us to deploy our instruments during the cruises of his project, and the crew of RV *Pelagia* for assistance in deployment and recovery of the instrumentation. We thank Leo Maas for helpful discussions and the anonymous reviewers for their constructive comments. J. G. has been supported by a European Community TMR research fellowship under contract MAS3-CT97-5047. This is NIOZ contribution number 3480.

## APPENDIX

### Estimation of heat flux bias

Measurements of velocity and temperature are not co-located in the given instrumentation set up. Hence, heat flux estimates from ADCP and thermistor string data may be severely biased. Following van Haren *et al.* (1994), the bias can be estimated as  $\Delta_{T_w} = d \tan \theta \overline{T' \partial \hat{w}' / \partial z} / 2$ , where  $d$  is half the beam spread of the ADCP. However, derivation of this correction term is based on the assumption that the spatial scale  $\delta$  of velocity variations are large compared to half the beam spread,  $\delta \gg d$ .

To test the validity of this assumption independently we extract the size of overturns in each temperature profile. The temperature overturn length scale is defined as the distance between consecutive local temperature minima. In total, close to  $2 \times 10^5$  overturns are detected. Figure A1 shows the distribution of overturn length scales normalized by half the beam spread at the height of the center of each overturn.

Assuming similar scales of velocity fluctuations and temperature fluctuations and, conservatively, a 1:1 aspect ratio, we find that in more than 70% of the cases the length scale of fluctuations is larger than half the beam spread,  $\delta > d$ . However, less than 40% of the overturns satisfy  $\delta > 2d$ . Therefore, the direct correlation method  $\overline{T' \hat{w}'}$  may bias the heat-flux estimate by approximately 2–3 times the error  $\Delta_{T_w}$  (see text).

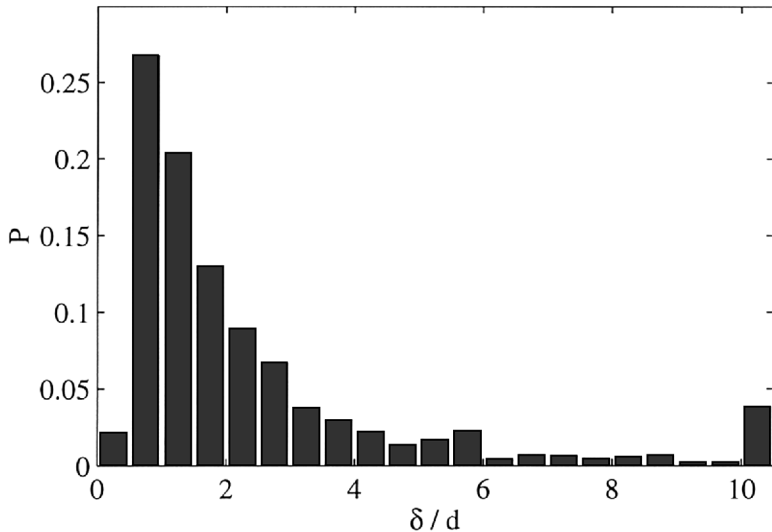


Figure A1. Distribution of length scale  $\delta$  of temperature fluctuations, normalized by half the beam spread  $d$ .

#### REFERENCES

- Armi, L. 1978. Some evidence for boundary mixing in the deep ocean. *J. Geophys. Res.*, *83*, 1971–1979.
- Armi, L. and R. C. Millard. 1976. The bottom boundary layer of the deep ocean. *J. Geophys. Res.*, *27*, 4983–4990.
- De Silva, I. P. D., J. Imberger and G. N. Ivey. 1998. Breaking of super-critically incident internal waves at a sloping bed *in* *Physical Processes in Lakes and Oceans, Coastal Estuar. Studies*, *54*, 475–484.
- Eriksen, C. C. 1985. Implications of ocean bottom reflection for internal wave spectra and mixing. *J. Phys. Oceanogr.*, *15*, 1145–1156.
- 1998. Internal wave reflection and mixing at Fiberling Guyot. *J. Geophys. Res.*, *103*, 2977–2994.
- Fleury, M. and R. G. Lueck. 1994. Direct heat flux estimates using a towed vehicle. *J. Phys. Oceanogr.*, *24*, 801–818.
- Gargett, A. E. and J. N. Moum. 1995. Mixing efficiency in turbulent tidal fronts: Results from direct and indirect measurements of density flux. *J. Phys. Oceanogr.*, *25*, 2583–2608.
- 1990. The role of secondary circulation in boundary mixing. *J. Geophys. Res.*, *95*, 3181–3188.
- Garrett, C. 1991. Marginal mixing theories. *Atmosphere-Ocean*, *29*, 313–339.
- Gemmrich, J. R. and H. van Haren. 2001. Thermal fronts generated by internal waves propagating obliquely along the continental slope. *J. Phys. Oceanogr.*, *31*, 649–655.
- Huthnance, J. M. and P. G. Baines. 1982. Tidal currents in the northwest African upwelling region. *Deep-Sea Res.*, *29*, 285–306.
- Ivey, G. N. and R. I. Nokes. 1989. Vertical mixing due to the breaking of critical internal waves on sloping boundaries. *J. Fluid Mech.*, *204*, 479–500.
- Kistovich, A. V. and Y. D. Chashechkin. 1993. The structure of transient boundary flow along an inclined plane in a continuously stratified medium. *J. Appl. Math. Mech.*, *57*, 633–639.

- Lohrmann, A., B. Hackett and L. P. Røed. 1990. High resolution measurements of turbulence, velocity and stress using a pulse to pulse coherent sonar. *J. Atmos. Ocean. Tech.*, *7*, 19–37.
- Lueck, R. G. and T. D. Mudge. 1997. Topographically induced mixing around a shallow seamount. *Science*, *276*, 1831–1833.
- Lueck, R. G. and F. Wolk. 1999. An efficient method for determining the significance of covariance estimates. *J. Atmos. Ocean. Tech.*, *16*, 773–775.
- Maas, L. R. M. and J. T. F. Zimmerman. 1989a. Tide-topography interactions in a stratified shelf sea. I. Basic equations for quasi non-linear internal tides. *Geophys. Astrophys. Fluid Dyn.*, *45*, 1–35.
- 1989b. Tide-topography interactions in a stratified shelf sea. II. Bottom trapped internal tides and baroclinic residual currents. *Geophys. Astrophys. Fluid Dyn.*, *45*, 37–69.
- Munk, W. H. 1966. Abyssal recipes. *Deep-Sea Res.*, *13*, 207–230.
- Phillips, O. M., J. H. Shyu and H. Salmun. 1986. An experiment on boundary mixing: Mean circulation and transport rates. *J. Fluid Mech.*, *173*, 473–499.
- Polzin, K. L., J. M. Toole, J. R. Ledwell and R. W. Schmitt. 1997. Spatial variability of turbulent mixing in the abyssal ocean. *Science*, *276*, 93–96.
- Slinn, D. N. and J. J. Riley. 1996. Turbulent mixing in the oceanic boundary layer caused by internal wave reflection from sloping terrain. *Dyn. Atmos. Ocean.*, *24*, 51–62.
- Sun, H., E. Kunze and A. J. Williams III. 1996. Vertical heat flux measurements from a neutrally buoyant float. *J. Phys. Oceanogr.*, *26*, 984–1001.
- Thorpe, S. A. 1987a. On the reflection of a train of finite-amplitude internal waves from a uniform slope. *J. Fluid Mech.*, *178*, 279–302.
- 1987b. Currents and temperature variability on the continental slope. *Philos. Trans. Roy. Soc. Lond.*, *A323*, 471–517.
- 1992. Thermal fronts caused by internal waves reflecting from a slope. *J. Phys. Oceanogr.*, *22*, 105–108.
- 1999. Fronts formed by obliquely reflecting internal gravity waves at a sloping bottom. *J. Phys. Oceanogr.*, *29*, 2462–2467.
- Toole, J. M., R. W. Schmitt, K. L. Polzin and E. Kunze. 1997. Near-boundary mixing above the flanks of a midlatitude seamount. *J. Geophys. Res.*, *102*, 947–959.
- Trowbridge, J. H. and S. J. Lentz. 1998. Dynamics of the bottom boundary layer on the northern Californian shelf. *J. Phys. Oceanogr.*, *28*, 2075–2093.
- van Haren, H. 2000. Comment on “An efficient method for determining the significance of covariance estimates.” *J. Atmos. Ocean. Tech.*, *17*, 885–886.
- van Haren, H., N. Oakey and C. Garrett. 1994. Measurements of internal wave band eddy fluxes above a sloping bottom. *J. Mar. Res.*, *52*, 909–946.
- van Haren, H., R. Groenewegen, M. Laan and B. Koster. 2001. A fast and accurate thermistor string. *J. Atmos. Ocean. Tech.*, *18*, 110–119.
- van Haren, J. J. M. 1990. Observations on the horizontal and vertical structure of currents at sub-tidal frequencies in the central North Sea. *Neth. J. Sea Res.*, *27*, 1–23.
- Yamazaki, H. and T. Osborn. 1993. Direct estimation of heat flux in a seasonal thermocline. *J. Phys. Oceanogr.*, *23*, 503–516.